Available online at www.sciencedirect.com

SciVerse ScienceDirect

Acta Materialia 60 (2012) 4540–4550

Acta MATERIALIA

www.elsevier.com/locate/actamat

A study of the mechanism of formation and numerical simulations of crack patterns in ceramics subjected to thermal shock

C.P. Jiang [a,*], X.F. Wu [a], J. Li [b], F. Song [c], Y.F. Shao [c], X.H. Xu [c], P. Yan [a]

[a] School of Aeronautic Science and Engineering, Beihang University, Beijing 100191, People's Republic of China
[b] LSPM, CNRS UPR 3407, Université Paris XIII, 99 Avenue Jean-Baptiste Clément, Villetaneuse 93430, France
[c] State Key Laboratory of Nonlinear Mechanics, Institute of Mechanics, Chinese Academy of Sciences, Beijing 100190, People's Republic of China

Received 15 December 2011; received in revised form 13 May 2012; accepted 14 May 2012
Available online 9 June 2012

Abstract

The present work examines the mechanism of formation of thermal shock crack patterns in ceramics. An attempt has been made to bridge the gap between theoretical predictions and experimental data. A set of experiments on thin ceramic specimens yielded two-dimensional readings of thermal shock crack patterns with periodical and hierarchical characteristics that vary with the thermal shock temperature. Based on the minimum potential energy principle the finite element method was used for numerical simulations, in which the temperature dependence of the material properties was considered. To overcome the difficulty of a lack of accurate data on the convective heat transfer coefficient at high temperatures, a "semi-inverse method" was developed, which explores a new method for estimating a physical quantity that is difficult to measure using physical quantities, which are relatively easy to measure. The numerical and experimental data were compared and discussed. The obtained numerical results are in good agreement with the experimental data. Furthermore, the numerical simulations can conveniently reproduce the evolution of thermal shock cracks, which is difficult to observe experimentally. In addition, some interesting phenomena related to thermal shock crack pattern evolution were observed. The present theoretical–numerical–experimental study has led to a much improved understanding of the formation and evolution of thermal shock crack patterns in ceramics.

Keywords: Ceramics; Thermal shock; Crack patterns; Numerical simulations; Semi-inverse method

1. Introduction

Due to their excellent high temperature mechanical properties, corrosion resistance, wear resistance, erosion resistance, and oxidation resistance ceramic materials have been widely used in various industries, especially in thermostructures such as gas turbine engines [1] for aircraft propulsion, power generation, marine propulsion, and thermal protection structures in hypersonic vehicles [2,3].

However, the inherent brittleness and lack of ductility of ceramic materials make them particularly susceptible to thermal shock failure, even catastrophic fracture. Research on the thermal shock failure of ceramics has been performed for more than half a century. In the 1950s Kingery [4] proposed the critical stress fracture theory, which requires that materials have a high tensile strength and low Young's modulus to avoid the initiation of fracture by thermal stress. Subsequently, Hasselman [5,6] proposed the thermal shock damage theory, which requires that materials have a low tensile strength and high Young's modulus to prevent cracks from propagating. Both theories have been extensively used, but some basic problems remain. Numerous theoretical and experimental studies on the thermal shock failure of ceramics have been conducted [7–15]. Among them, Hasselman [7] provided qualitative theoretical predictions of the crack propagation behavior of polycrystalline alumina rods under thermal shock caused by water quenching. Lu and Fleck [9] analyzed the thermal shock resistance of brittle solids using a

* Corresponding author. Tel.: +86 010 82317507.
E-mail address: jiangchiping@buaa.edu.cn (C.P. Jiang).

1359-6454/$36.00 © 2012 Acta Materialia Inc. Published by Elsevier Ltd. All rights reserved.
http://dx.doi.org/10.1016/j.actamat.2012.05.020

stress-based fracture criterion for a plate containing a distribution of flaws, such as pores, and a critical stress intensity factor criterion for a plate containing a single dominant crack aligned with the through thickness direction. Collin and Rowcliffe [11] studied the thermal shock behavior of brittle materials using the indentation quench method, obtained crack growth vs. temperature curves, and derived an expression for predicting the thermal shock resistance. Han and Wang [15] conducted thermal shock studies for three typical thermal shock specimens and demonstrated the significance of incorporating temperature-dependent material properties for the thermal shock resistance of ceramics for high temperature applications.

Although great progress has been achieved in studying the thermal shock failure of ceramics, it is still largely insufficient for practical engineering needs; designing ceramics has to be approached statistically, and proof testing is still a frequently used technique to guarantee the minimum service life of a ceramic component [1]. It is recognized that a basic understanding of the thermal shock failure mechanism must be gained to achieve the full potential of ceramics.

Researchers very early noticed that thermal shock cracks exhibit generally regular and elegant patterns, such as periodical and hierarchical characteristics, which are of practical importance for a clear understanding of the thermal shock failure mechanism of ceramics. Bažant [16] and Nemat-Nasser et al. [17,18] studied the stability of propagated thermal shock cracks (or drying shrinkage cracks) using the energy principle, and they theoretically discussed the length hierarchy phenomenon. Bahr et al. [19–21] theoretically and experimentally studied thermal shock crack patterns. Jenkins [22] used a method based on energy minimization to determine the spacing and penetration of a regular array of cracks in a shrinking slab due to a changing temperature field. Recently Bourdin et al. [23] surveyed the variational approach to fracture. The authors stated that the variational approach addresses crack initiation and crack propagation in a united framework. The total energy in a body is the sum of the elastic energy and the Griffith's surface energy associated with the cracks. The authors addressed three main issues, initiation, irreversibility, and path, which have plagued fracture mechanics over the last 100 or so years. Based on this variational approach, efficient numerical algorithms were developed which are capable of performing rather complicated fracture analyses in brittle materials. Furthermore, numerical studies for predicting cracks induced by thermal stresses were also performed [24].

However, no quantitative predictions of thermal shock crack patterns in practical materials have been reported to date. There are two main difficulties in predicting thermal shock crack patterns. The first is the temperature dependence of the material properties. From Fig. 8 in Section 4 it can be seen that for 99% Al_2O_3 ceramics the thermal conductivity, specific heat, and coefficient of thermal expansion possess steep non-linear temperature dependencies. Apparently, the assumption of constant material properties cannot yield accurate quantitative predictions. The second is the lack of accurate data on the material properties at high temperatures. The available data [33–36] on effective heat transfer coefficients are disperse, with the consensus being between 10^4 and $10^5\ W\ m^{-2}\ K^{-1}$. Such dispersion prohibits an accurate quantitative study.

This work constitutes a continuing study in the quest to elucidate the mechanism of formation and undertake quantitative numerical simulations of thermal shock crack patterns in ceramics. To overcome the above mentioned difficulties, a new approach combining experiments with numerical simulations has been explored and developed. This paper is organized as follows.

Section 2 reports a set of thermal shock experiments using 99% Al_2O_3 ceramics, in which thin specimens exhibit rather regular thermal shock through crack patterns, and the dispersion of the crack spacing is small at the same thermal shock severity. Section 3 formulates the basic thermal stress theory, and the minimum potential energy principle that is used to predict thermal shock crack patterns. Section 4 develops a numerical simulation of thermal shock cracks, where the effective heat transfer coefficient is estimated inversely from the crack spacing; in turn, the length and hierarchy of the thermal shock cracks are quantitatively predicted. Section 5 is a comparison of the numerical and experimental results with a discussion of the results. The emphasis is on the mechanism of formation of thermal shock crack patterns. Finally, several conclusions are drawn in Section 6.

2. Experimental

The study on the mechanism of formation of thermal shock crack patterns requires high accuracy measurements of the crack geometry, thus two-dimensional through cracks are highly desirable. To this end 99% Al_2O_3 powder (University of Science and Technology Beijing Experimental Factory Co., Beijing, China) was thermoformed into $50 \times 10 \times 1$ mm thin specimens. The specimens were then polished and tightly stacked together in sets of five, with two thick ceramic plates on the outside to prevent the temperature distribution from being disturbed by coolant accessing the interior surfaces of the specimens. Finally, the stacks of alumina plates were bound with inconel wires positioned 3–4 mm from the ends of the specimens, as shown in Fig. 1.

The bound specimens were heated in a furnace at a rate of $10\ °C\ min^{-1}$ to the preset temperature T_0 and

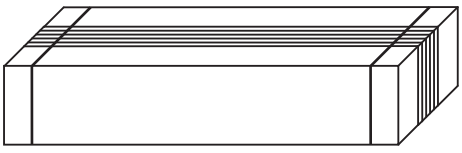

Fig. 1. Bound specimens for thermal shock.

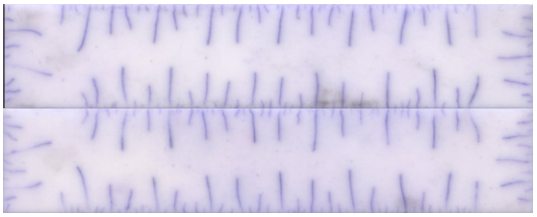

Fig. 2. Both sides of a specimen after thermal shock at $T_0 = 400$ °C.

maintained at this temperature for approximately 30 min. The range of T_0 was from 300 to 600 °C, with an interval of 100 °C. It will be observed from the later experiments that there is a dramatic change in the thermal shock crack patterns between $T_0 = 300$ °C and $T_0 = 400$ °C. Such a phenomenon may imply dramatic changes in the relevant material properties, therefore, $T_0 = 350$ °C was added. After heating the heated specimens were dropped into a water bath at $T_\infty = 20$ °C by free fall while continuously stirring the cooling water. The specimens were removed from the water bath 10 min later and dried, then dyed with blue ink to observe the cracks formed.

It was observed that the thermal shock cracks passed through and were perpendicular to the top or bottom face, with reference to the digitally scanned photographs of a specimen after thermal shock at $T_0 = 400$ °C (Fig. 2), where the crack patterns on both of the sides of the specimen were identical. At various values of T_0 (from 300 to 600 °C) this feature remained unchanged. The two-dimensional crack patterns are convenient for measuring crack geometry and thermal stress analysis and, consequently, for a thorough study of the mechanism of formation of crack patterns.

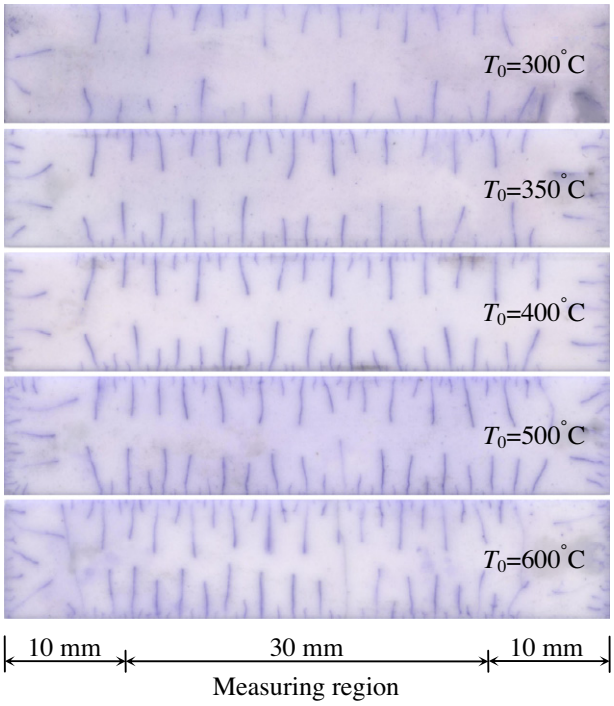

Fig. 3. Specimens after thermal shock at various values of T_0.

Table 1
Variations in the dimensionless crack spacing $\bar{s} = s/L_c$ with thermal temperature T_0, where s is the crack spacing and $L_c = 5$ mm is half of the specimen width.

T_0 (°C)	$\bar{s} = s/L_c$					
	No. 1	No. 2	No. 3	No. 4	No. 5	Average
300	0.335	0.342	0.272	0.314	0.338	0.320
350	0.172	0.194	0.173	0.170	0.210	0.184
400	0.173	0.156	0.159	0.162	0.161	0.162
500	0.143	0.142	0.143	0.136	0.145	0.142
600	0.128	0.134	0.109	0.118	0.111	0.120

Furthermore, it was observed that the crack patterns (spacing, length, length hierarchy, and periodicity) were similar in the five specimens at each value of T_0, whereas the crack patterns evolved with an increase in the thermal shock temperature T_0. The higher T_0, the less crack spacing there was. In addition, the long cracks became longer and the short cracks became shorter as T_0 increased, as shown in Fig. 3.

In measuring the geometry of the thermal shock cracks, to remove the effects of the end boundaries, the regions within 10 mm from the two ends of the specimens were excluded, as shown in Fig. 3. The average dimensionless spacing $\bar{s} = s/L_c$ of the thermal shock cracks in a specimen was easy to measure, where s is the crack spacing and $L_c = 5$ mm is half of the specimen width. The variations in the dimensionless crack spacing $\bar{s}$ with the thermal shock temperature T_0 for all specimens are presented in Table 1. It can be seen that at each value of T_0 the fluctuation in the average crack spacing among the five specimens was very small, and the maximum deviation from the total average value was less than 10%, except for a very small number of specimens with a slightly larger deviation.

To investigate the crack length distribution we introduced a dimensionless crack length, $\bar{p} = p/L_c$, where p is the crack length. The histogram of the frequency distribution of $\bar{p}$ at $T_0 = 400$ °C is shown in Fig. 4, where the range of $\bar{p}$, namely 0–1, is divided into 50 equal parts. The histograms at various values of T_0 refer to Fig. 14 in Section 5.

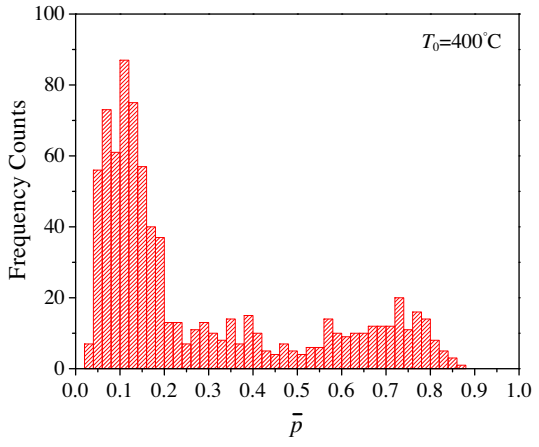

Fig. 4. Histogram of the dimensionless crack length ($\bar{p} = p/L_c$) distribution in the measurement region at the thermal shock temperature $T_0 = 400$ °C.

From the shocked specimens (Figs. 2 and 3) and their measurements (Fig. 4 and Table 1) it can be seen that the length and distribution of the thermal shock cracks exhibit an interesting elegant regularity (such as periodical and hierarchical characteristics). In the following sections the theoretical and numerical approaches will be developed to gain a scientific understanding of the mechanism of formation and evolution of thermal shock crack patterns.

3. Theoretical considerations

3.1. Model

Using the measurement region of the specimen (Fig. 3) as the analytical model $A_1A_2A_3A_4$, as shown in Fig. 5, where the ceramic material is assumed to be homogeneous and isotropic, the random effects induced by the microstructural heterogeneity and other uncertainties will be considered in Section 5.

3.2. Temperature and thermal stress fields

A Cartesian coordinate system Oxz in the model in Fig. 5, where the origin is at the center of the region, was established. Noting that the water temperature holds at $T_\infty = 20$ °C during the water quenching process and that the effect of the end boundaries of the measurement region is precluded, the temperature field $T = T(z, t)$ is one-dimensional (z-direction). The heat conduction equation can be written as [25]:

$$\frac{\partial}{\partial z}\left[k(T)\cdot\frac{\partial T}{\partial z}\right] = \rho(T)\cdot c(T)\cdot\frac{\partial T}{\partial t} \tag{1}$$

where t is the time and $k(T)$, $\rho(T)$, and $c(T)$ are the temperature-dependent thermal conductivity, density, and specific heat, respectively. The initial thermal condition can be written as:

$$T(z,t)|_{t=0} = T_0 \tag{2}$$

where T_0 is the preset temperature of thermal shock with values of 300, 350, 400, 500, and 600 °C, respectively. Noting that the x-axis is a symmetrical axis of temperature and that both ends of the model can be regarded as being thermally insulated, the boundary condition of the upper half model can be written as [25]:

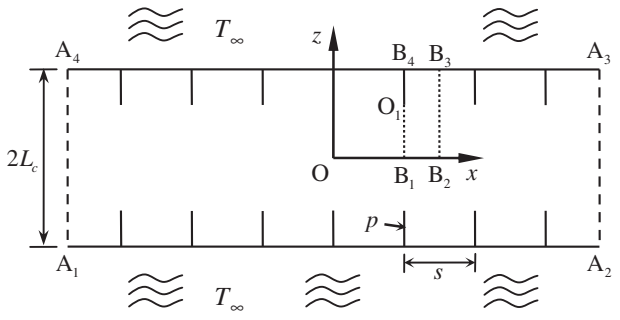

Fig. 5. Analytical model of the measurement region.

$$\begin{cases} \frac{\partial T}{\partial z} = 0 & \text{on the } x\text{-axis} \\ -k(T)\cdot\frac{\partial T}{\partial z} = h(T)\cdot[T(L_c,t) - T_\infty] & \text{on } A_4A_3 \\ \frac{\partial T}{\partial x} = 0 & \text{on } A_1A_4 \text{ and } A_2A_3 \end{cases} \tag{3}$$

where $h(T)$ is the temperature-dependent convective heat transfer coefficient.

The transient temperature field $T = T(z, t)$ in the model can be obtained from Eqs. (1)–(3). The stress field at any time point can then be obtained using thermo-elastic theory. Despite the one-dimensional temperature field, no analytical expressions of the temperature and thermal stress fields are available, because of the non-linear temperature dependence of the material properties of ceramics. In this work the software ANSYS was employed to calculate the temperature and thermal stress fields.

3.3. Optimal crack patterns

Griffith's theory of fracture addresses the initiation and propagation of cracks in a unified variational framework [22,23]. The cracking path is an issue that has plagued fracture mechanics for a long time [23]. Because the analytical model of the specimens is homogeneous and isotropic, during the initial stages it was assumed that the thermal shock cracks were of equal length and equal spacing and perpendicular to the boundary, as shown in Fig. 5. This assumption was verified by our experiments (Fig. 3). As a consequence of this result, the thermal shock cracks do not disturb the transient temperature field, but change the transient stress field in the specimens. The strain energy U in the specimen can be written as:

$$U = U(s,p,t) \tag{4}$$

where s and p are the spacing and length of the thermal shock cracks, respectively. Assuming that the surface energy S, which is the energy required to form new crack surfaces, is proportional to p this expression can be written as:

$$S = \gamma p \tag{5}$$

where γ is the surface energy density. The total potential energy of the analytical model can be written as:

$$W(s,p,t) = U + S \tag{6}$$

By considering the periodicity and symmetry of the model with cracks the rectangular region $O_1B_1B_2B_3B_4$ in Fig. 5 can be used as a computational region, where O_1B_4 is the crack face, B_2B_3 is the perpendicular bisector, and B_1B_2 is located on the symmetrical axis Ox. In the computational region the average total potential energy of the unit area can be written as:

$$\overline{W}(s,p,t) = \frac{W}{L_c\cdot(s/2)} \tag{7}$$

According to the minimum potential energy principle, optimal crack patterns minimize the average total potential energy of the unit area. Let s_0 and p_0 be the spacing and length of the optimal thermal shock cracks, respectively, at time t_0, then we have

$$\overline{W}(s_0, p_0, t_0) = \min \overline{W}(s, p, t_0) \tag{8}$$

As an illustrative example take $T_0 = 400$ °C and observe the location change of the minimum value on the curved surface of $\overline{W}$ during the thermal shock process. It is observed that when the thermal shock time t is less than a certain critical time t_c the minimum value on the curved surface of $\bar{W}$ is located at $\bar{p}_0 = p_0/L_c = 0$, as shown in Fig. 6a, which indicates that the specimen does not crack. However, when $t > t_c$ the minimum value shifts to $\bar{s} = \bar{s}_0 = s_0/L_c$ and $\bar{p} = \bar{p}_0 = p_0/L_c$, as shown in Fig. 6b, which indicates that s_0 and p_0 are the optimal crack spacing and length, respectively.

Now consider the evolution of thermal shock crack patterns with time. Theoretically, during the thermal shock process the average total potential energy curved surface changes continuously with time. Consequently, the idealized optimal crack spacing and length (s_0, p_0) also change continuously with time. As an illustrative example, the idealized curve of $\bar{s}_0$ vs. time at $T_0 = 400$ °C is plotted by a solid line in Fig. 7. It can be observed that the idealized optimal crack spacing rapidly reaches its theoretical minimum, then increases. However, the cracks formed do not recede or disappear, which prevents the crack spacing from changing continuously with time. The crack spacing should

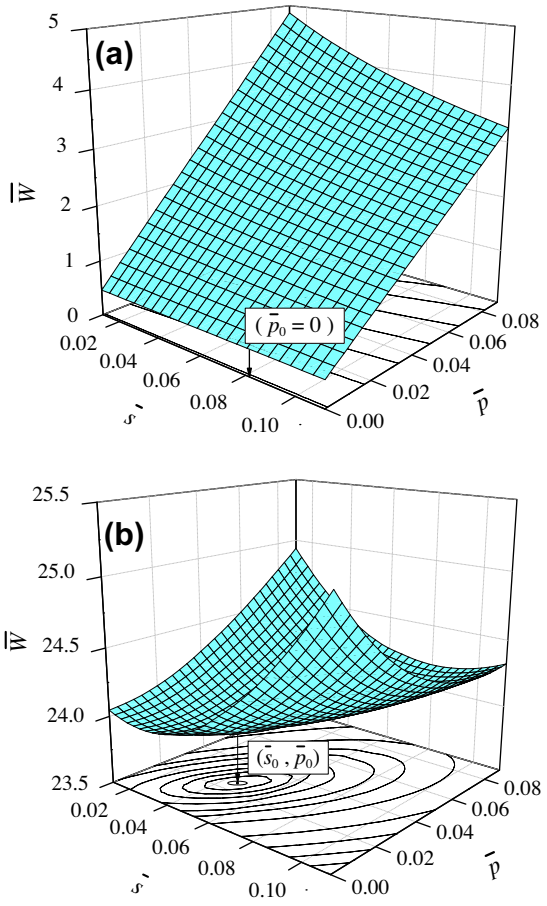

Fig. 6. Graphs of the average total potential energy curved surfaces for two time points at $T_0 = 400$ °C.

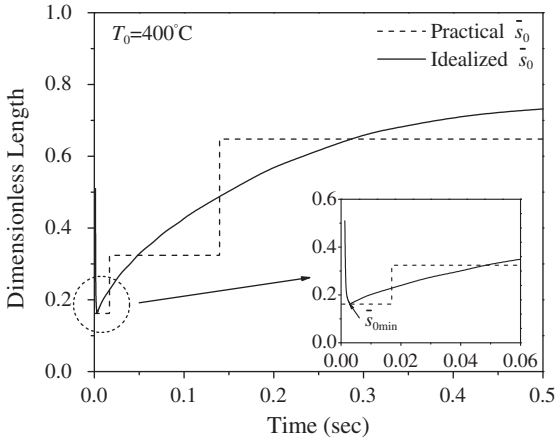

Fig. 7. The idealized continuous curve and practical hierarchical broken line of the optimal crack spacing vs. time at $T_0 = 400$ °C.

rapidly reach a minimum $\bar{s}_{0\,min}$ (in the vicinity of the theoretical minimum) due to the appearance of additional cracks. The cracks then continue to propagate while maintaining a constant spacing until the minimum point of the potential energy jumps to a curve representing "spatial period doubling" [22], i.e. every second crack continues to propagate, whereas the other cracks stop. The process can be repeated and forms a hierarchical crack pattern. The practical hierarchical crack spacing is shown by the dashed line in Fig. 7. It can be seen that the practical hierarchical spacing approaches the idealized spacing by stepping, with the restraint of "spatial period doubling".

4. Numerical simulations

4.1. Semi-inverse method

The finite element software ANSYS was used for the numerical simulations, in which the main challenge arises from the temperature dependence of the material properties and the difficulties associated with measuring these properties at high temperatures.

From the available data the Young's modulus E [26], the Poisson ratio ν [26], the density ρ [26], and the surface energy density γ [27] of 99% Al_2O_3 ceramics are listed in Table 2.

Because the thermal expansion coefficient of ceramics is very small the density ρ can be regarded as being temperature-independent. Fukuhura and Yamauchi [28] experimentally studied the temperature dependence of the Young's modulus E and the Poisson ratio ν for alumina and reported that they remain approximately unchanged in the range 20–600 °C. An experimental report by de Smet

Table 2
Four material properties of 99% Al_2O_3 ceramics.

E (Gpa)	ν	ρ (kg m^{-3})	γ (J m^{-2})
370	0.22	3980	12.16

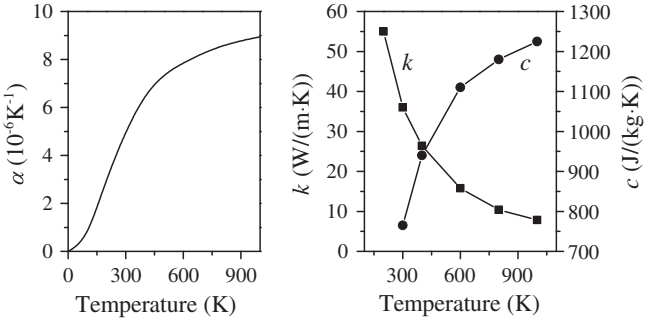

Fig. 8. Graphs of the thermal conductivity k [30], the specific heat c [31], the coefficient of thermal expansion α [32] of 99% Al_2O_3 ceramics vs. temperature.

and Bach [29] showed that the fracture toughness K_{IC} of two types of alumina differ slightly at 20 and 600 °C. Based on fracture mechanics $2\gamma = K_{IC}^2/E$, thus the surface energy density γ can also be regarded as being temperature-independent in this temperature range.

However, the thermal conductivity k, the specific heat c, and the thermal expansion coefficient α are strongly temperature-dependent, as shown in Fig. 8.

The biggest challenge in numerical simulations arises from a lack of accurate data on the convective heat transfer coefficient in thermal shock. From the available data [33–36] the mutual deviation is high, up to one order of magnitude (10^4–10^5 W m^{-2} K^{-1}). In fact, this large dispersion prevents accurate quantitative analysis. To overcome this difficulty let us examine Table 1.

It can be seen that the fluctuation in the average crack spacing among the five specimens at each thermal shock temperature was small, at the same time it is easy to measure. Therefore this work explores and develops a new semi-inverse method combining experimental data and numerical simulations, i.e. the convective heat transfer coefficient is inversely estimated from the thermal shock crack spacing. The crack length, hierarchical characteristics, and their evolution are then numerically predicted. It will be seen that although the presently developed semi-inverse method is not a quantitative prediction method in the complete sense, it has led to a much improved understanding of the mechanism of formation of thermal shock crack patterns. Furthermore, the semi-inverse method provides a new method for estimating a physical quantity that is difficult to measure using physical quantities, which are easy to measure.

4.2. Computational region

From the theoretical considerations in the last section it can be seen that during the initial stages of thermal shock cracking all periodically distributed cracks propagate uniformly. Based on this fact, we defined a fundamental region with a minimum period, as shown in Fig. 9a, where $s_{0\min}$ is the minimum crack spacing (which can be predicted, but in this work, to inversely estimate the convective heat transfer

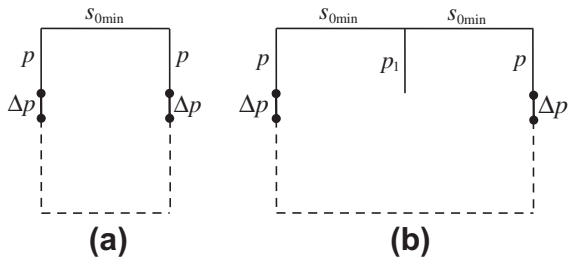

Fig. 9. Fundamental region with the minimum period: (a) for equal length cracks during the initial stage; (b) for cracks of two length levels.

coefficient, the values are taken from experimental data), p is the crack length and Δp is the small propagation value within a small time interval Δt. According to the symmetry the rectangular region $O_1B_1B_2B_3B_4$ in Fig. 5 (see also Fig. 9) can be used as a computational region, as shown in Fig. 10a. When the minimum point of the potential energy jumps to a certain curve of "spatial period doubling" every second crack continues to propagate, whereas the other cracks stop (with a length of p_1). The fundamental region is extended in Fig. 9b and the corresponding computational region is extended in Fig. 10b. The process can be repeated for multilevel crack patterns.

According to the periodicity and symmetry of the thermal shock cracks the displacement boundary conditions of the computational region can be prescribed as shown in Fig. 10. The crack surfaces are traction free.

4.3. Numerical simulations

4.3.1. Finite element mesh and time step

In the process of calculating numerical solutions the average total potential energy of the unit area needs to be accurately calculated, therefore a fine mesh is employed in the computational region. Because of the large temperature gradient in the vicinity of the line B_3B_4 and the stress singularity at the crack tip finer meshes are used in these regions.

Based on our experience, the calculation time was set to 1 s, which was uniformly divided into 500 time steps. Dur-

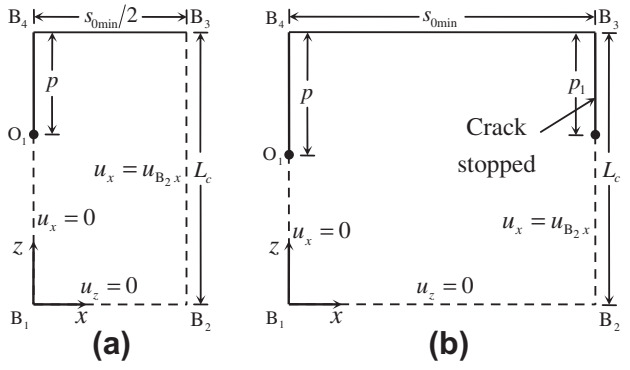

Fig. 10. Computational regions and their displacement boundary conditions.

ing the first 0.1 s, when the large variation in the temperature distribution was considered, the time steps were increased from 50 to 500.

4.3.2. Estimation of the effective heat transfer coefficient

Let us now estimate the heat transfer coefficient h inversely from the crack spacing. For any value of h finite element calculations can provide the corresponding temperature and stress fields, then providing the crack spacing $s_{0\min}$ using the minimum potential energy principle. The variations in the dimensionless crack spacing $\bar{s}_{0\min}$ with the heat transfer coefficient h at $T_0 = 400$ °C are shown in Fig. 11. The value of h corresponding to the practical crack spacing is called the effective heat transfer coefficient, which is used to predict the following evolution of the crack pattern. For example, from the experiments the dimensionless crack spacing is $\bar{s} = 0.162$ at $T_0 = 400$ °C (see Table 1). Then, from Fig. 11, the corresponding effective heat transfer coefficient is $\bar{h}_{T_0=400\ ^\circ\mathrm{C}} = 86{,}000\ \mathrm{W\ m^{-2}\ K^{-2}}$. The values of the effective heat transfer coefficient $\bar{h}$, derived by the semi-inverse method at various values of T_0, are listed in Table 3. The fitting curve of the effective heat transfer coefficient $\bar{h}$ vs. the thermal shock temperature T_0 is plotted in Fig. 12. It can be seen that the effective heat transfer coefficient first rapidly increases, then decreases. The tendency of variation is in agreement with the existing data [33–36], which indicate the potential for the application of the semi-inverse method. It can be used to estimate a physical quantity that is difficult to measure directly using physical quantities, which are easy to measure. Fig. 12 also reveals that there is a dramatic change in the thermal shock crack patterns between $T_0 = 300$ and $T_0 = 400$ °C (see Fig. 3 and Table 1), which corresponds to the peak of the effective heat transfer coefficient.

4.3.3. Numerical simulation results

The above developed method can simulate the evolution of thermal shock cracks. It has been shown that the process can be divided into two stages for $T_0 = 300$ °C and three stages for $T_0 = 350$, 400, 500, and 600 °C. The variations in the dimensionless crack spacing $\bar{s} = s/L_c$ and the dimensionless crack length $\bar{p} = p/L_c$ with time t are plotted in Fig. 13, where the solid lines represent the dimensionless spacing of the propagating cracks in various stages and the dashed lines represent the dimensionless lengths of the propagating cracks in various stages.

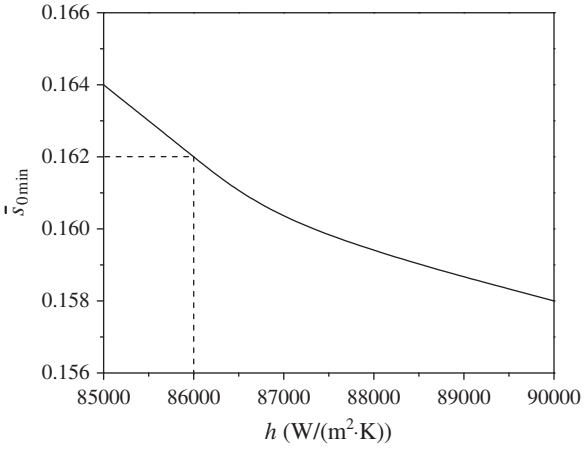

Fig. 11. Variations in the dimensionless crack spacing $\bar{s}_{0\min}$ with the heat transfer coefficient h at $T_0 = 400$ °C.

Table 3
Effective heat transfer coefficients $\bar{h}$ derived by the semi-inverse method at various values of T_0.

	T_0 (°C)				
	300	350	400	500	600
$\bar{h}$ (W m^{-2} K^{-1})	54,500	100,000	86,000	57,000	45,000

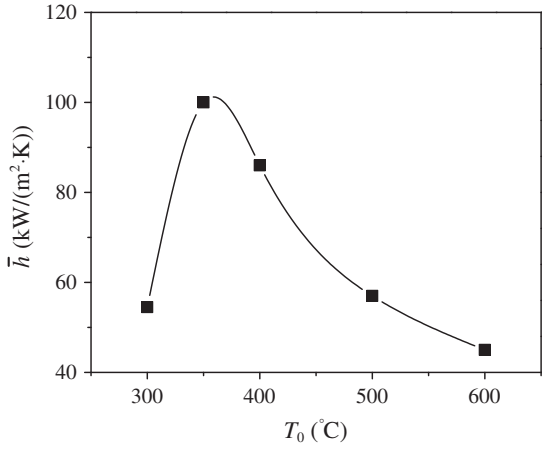

Fig. 12. Curve of the effective heat transfer coefficient $\bar{h}$ at various values of T_0.

In stage I the thermal shock cracks initiate and propagate uniformly with an equal spacing $\bar{s} = \bar{s}_1$. At first the thermal shock cracks propagate very rapidly, then the propagation speed decreases gradually with the release of thermal stress until the strain energy cannot support the simultaneous propagation of all cracks. At this moment the minimum point of the potential energy jumps to a certain curve of "spatial period doubling", i.e. every second crack continues to propagate, whereas the other cracks stop (see Section 3.3). The stationary cracks with a length of $\bar{p}_1$ are termed level I cracks. The evolution of crack patterns then continues to stage II.

In stage II the cracks with an equal spacing $\bar{s} = \bar{s}_2 = 2\bar{s}_1$ continue to propagate uniformly. At first the crack propagation speed shows a sudden increase because the strain energy supports propagation of only half of the cracks, then the propagation speed gradually decreases with the release of thermal stress until the strain energy cannot support simultaneous propagation of all propagating cracks in stage II. At this moment the minimum point of the potential energy again jumps, and every fourth crack continues to propagate, whereas the other cracks stop. The cracks which stop propagating at the end of stage II are termed level II cracks with a length

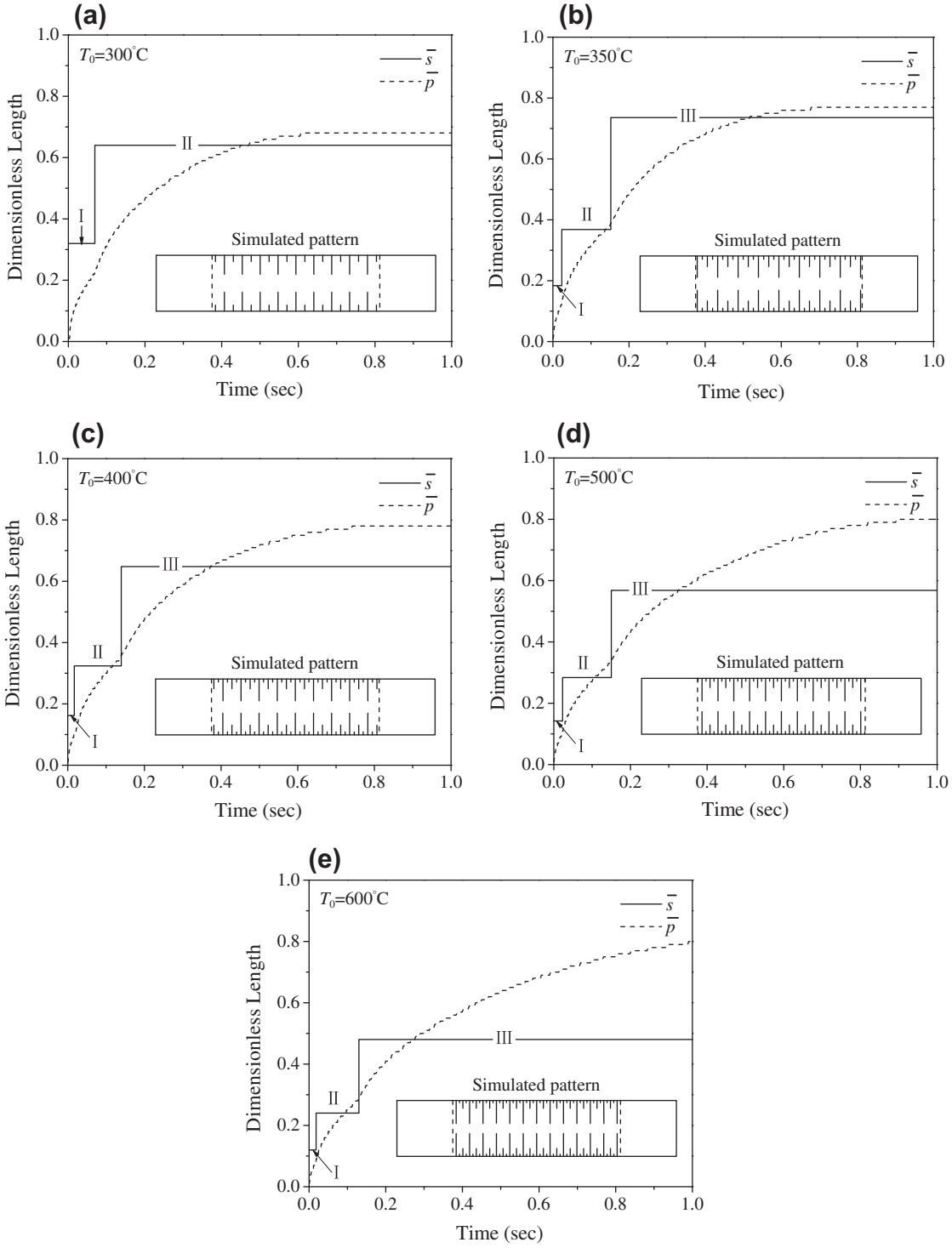

Fig. 13. Evolution of the thermal shock crack patterns reproduced by numerical simulations at various values of T_0.

$\bar{p}_2$, and then evolution of the crack patterns goes to stage III. This process can be repeated until the strain energy induced by thermal stress cannot support the propagation of any cracks.

The simulation results of the final crack patterns at various values of thermal shock temperature T_0 are listed in Table 4, where the long cracks for $T_0 = 300$ °C are classified as level III cracks, which will be explained below.

5. Comparison and discussion

The evolution of thermal shock cracks is difficult to observe experimentally, whereas it can be conveniently reproduced by numerical simulations. It is of interest to compare the numerical simulations and the experimental data. The theoretical, numerical, and experimental studies complement each other.

Table 4
Simulation of crack patterns at various values of T_0, where $\bar{s} = \bar{s}_1$ is the dimensionless spacing, $\bar{p}_1$, $\bar{p}_2$, and $\bar{p}_3$ denote the dimensionless lengths of levels I, II, and III, respectively.

	T_0 (°C)				
	300	350	400	500	600
$\bar{s}$	0.320	0.184	0.162	0.142	0.120
$\bar{p}_1$	0.22	0.12	0.11	0.1	0.08
$\bar{p}_2$	–	0.38	0.35	0.33	0.28
$\bar{p}_3$	0.68	0.77	0.78	0.81	0.82

5.1. Evolution of crack patterns

The numerical simulations precisely predict the periodical and hierarchical crack patterns, as shown in Fig. 13 and Table 4. The simulations show that once the thermal shock cracks initiate the longest level III cracks penetrate to a considerable distance. Then the level III crack (the longest crack) length increases slowly with increasing thermal shock temperature T_0, but will not reach half of the specimen width, i.e. L_c. In contrast, the lengths of the shortest level I cracks and the shorter level II cracks decrease with increasing T_0. Such laws, predicted by numerical simulations (Fig. 13 and Table 4), are in good agreement with the experimental observations (Fig. 3).

It is of especial interest to examine the evolution of the thermal shock crack hierarchy with thermal shock temperature T_0. The numerical simulations show that there are two crack levels at $T_0 = 300$ °C, and three levels of cracks at $T_0 = 350$ °C. During the transition process the embryonic third level cracks are located between, but not outside, the two developed crack levels. Therefore, at $T_0 = 300$ °C "level II" is reserved for the embryonic third level cracks, whereas the longer of the two developed levels of cracks is termed "level III". From Figs. 3 and 13 and Table 4 this classification captures the evolution characteristics of the thermal shock crack patterns with respect to the thermal shock temperature T_0.

5.2. Random effects

The thermal shock crack patterns predicted by the numerical simulations have strict periodical and hierarchical characteristics, whereas the experiments exhibit some degree of uncertainty. Fig. 14 presents histograms of the experimental data, which show the frequency distribution of the dimensionless crack length $\bar{p} = p/L_c$ at various thermal shock temperatures T_0. In these histograms $\bar{p}$ is divided into 20 equal parts for $T_0 = 300$ °C due to the small number of cracks, but into 50 equal parts for other values of T_0. For convenience of comparison the predicted lengths for every level ($\bar{p}_1$,$\bar{p}_2$, and $\bar{p}_3$) are also shown in Fig. 14 by the dashed-dotted lines. It can be seen that the numerical simulations predict three distinct levels of thermal shock cracks, whereas the statistical experimental data exhibit a random distribution with three peaks. This difference indicates that random effects, caused by the ceramic microstructural heterogeneity, experimental non-deterministic factors, and so on, must be considered.

Assuming that each crack level obeys a Gaussian distribution, then the entirety can be described by a composite Gaussian function:

$$y = \sum_{1}^{n} \frac{A_n}{B_n} e^{\frac{(x-x_n)^2}{2B_n^2}} \tag{9}$$

where $n = 2$ or 3 is the crack level number, the mean value of the Gaussian distribution x_n denotes the theoretical length of level n, and A_n and B_n are constants related to the amplitude and standard deviation, respectively.

Fitting the experimental data (the solid curves in Fig. 14) to the composite Gaussian function (Eq. (9)) it can be seen that the experimental data are in reasonable agreement with the numerical predictions, except for $T_0 = 300$ °C. At $T_0 = 300$ °C the numerical simulations predict two crack levels, but the experimental data seem to exhibit three "peaks". A reasonable explanation seems to be the effect of the embryonic level of the cracks (see Section 5.1). In addition, there are more random effects during the transition in crack patterns (from two to three crack levels).

6. Conclusions

(1) On visual observation thin alumina ceramics specimens after water quenching exhibit temperature-dependent crack patterns with rather regular periodic and hierarchical characteristics. The higher the temperature, the less the crack spacing and the larger the difference in crack length. At the same thermal shock temperature the dispersion in the number of cracks (or the average crack spacing) in various specimens is small, and the crack length distribution is the same from a statistical standpoint. The frequency counts vs. crack length histograms exhibit several peaks, which correspond to different crack lengths.

(2) Based on the minimum potential energy principle, the finite element method was used for numerical simulations. The temperature dependence of the material properties was considered to enable quantitative predictions of the thermal shock crack patterns. To overcome the difficulty of a lack of accurate data on the convective heat transfer coefficient at high temperatures (the dispersion is high up to one order of magnitude) a "semi-inverse method" was developed. The convective heat transfer coefficients were inversely estimated from the measured crack spacing at each temperature. It can be seen that the tendency for a variation in the effective convective heat transfer coefficient estimated by the semi-inverse method is in agreement with the existing data. The semi-inverse method is also an exploration of a new method to

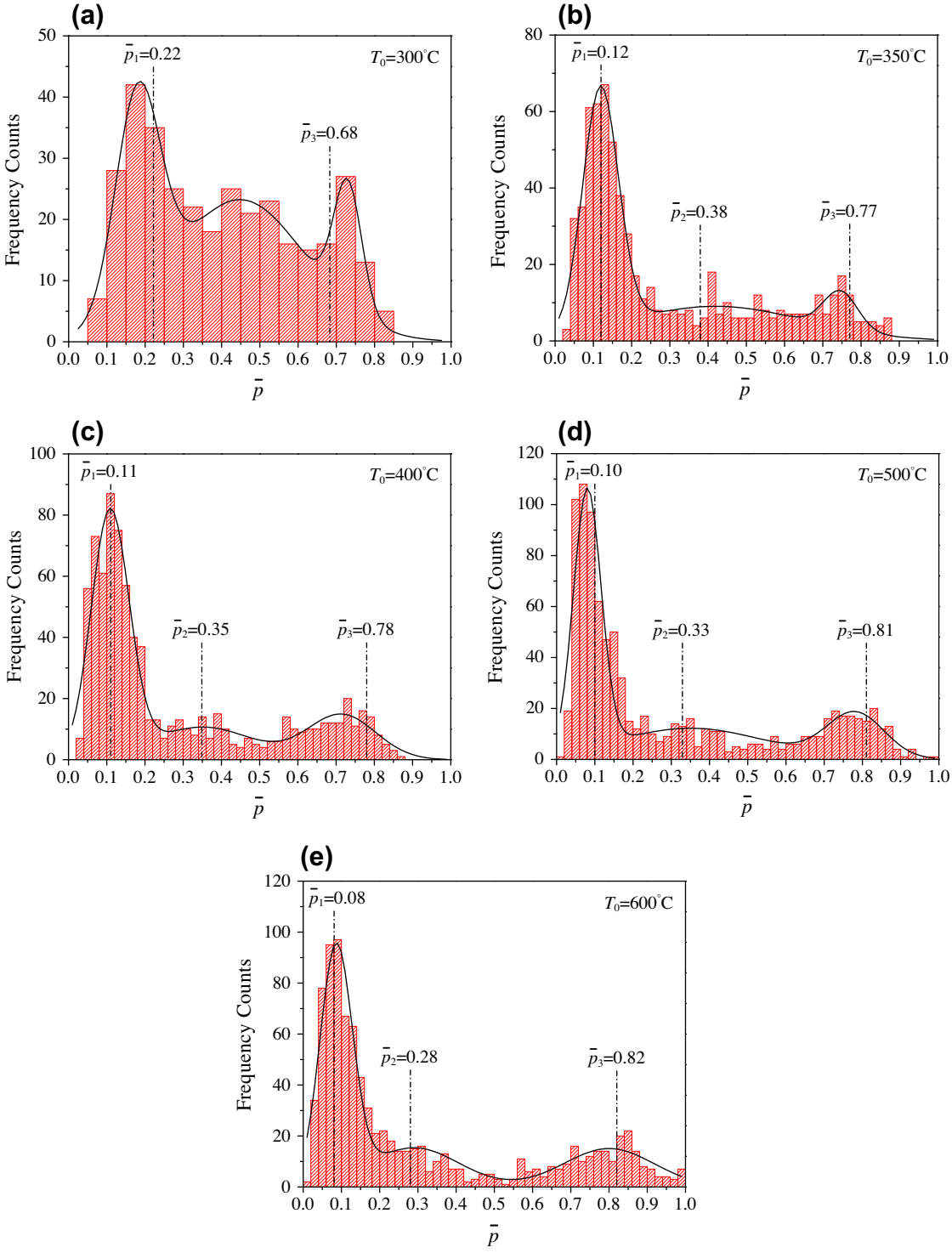

Fig. 14. Histograms of the dimensionless crack length ($\bar{p} = p/L_c$) distribution at various values of T_0, where the curves are the fitted results using the composite Gaussian function, and $\bar{p}_1$, $\bar{p}_2$, and $\bar{p}_3$ are the dimensionless lengths of three crack levels from numerical simulations.

overcome the difficulties in measuring high temperature material properties, i.e. to estimate a physical quantity that is difficult to measure using physical quantities which are easy to measure.

(3) The numerical simulations and experiments complement each other. The numerical simulations reveal the periodical and hierarchical characteristics of thermal shock cracks. Considering the random effects of crack length with a Gaussian distribution function, each crack level in the specimens can be distinctly separated. The numerical simulations can conveniently reproduce the evolution of thermal shock cracks, which is difficult to observe experimentally. It was found that with an increase in the thermal

shock temperature the initiating crack level appears between the developed crack levels; the length of the longest crack level continues to increase, whereas the other crack levels become shorter. These interesting phenomena were experimentally confirmed. The present theoretical–numerical–experimental study has led to a much improved understanding of the formation and evolution of thermal shock crack patterns in ceramics.

Acknowledgements

This work was supported by the National Natural Science Foundations of China (Grants Nos. 11061130550 and 11172023), the Fundamental Research Funds for the Central Universities and funding from the French ANR program T-Shock OTP J11R087.

References

[1] Padture NP, Gell M, Jordan EH. Science 2002;296:280–4.
[2] Levine SR et al. J Eur Ceram Soc 2002;22(14/15):2757–67.
[3] Opeka MM, Talmy IG, Zaykoski JA. J Mater Sci 2004;39(2):5887–904.
[4] Kingery WD. J Am Ceram Soc 1955;38(1):3–15.
[5] Hasselman DPH. J Am Ceram Soc 1963;46(11):535–40.
[6] Hasselman DPH. J Am Ceram Soc 1969;52(11):600–4.
[7] Hasselman DPH. J Am Ceram Soc 1970;53(9):490–5.
[8] Gupta TK. J Am Ceram Soc 1972;55(5):249–53.
[9] Lu TJ, Fleck NA. Acta Mater 1998;46(13):4755–68.
[10] Sherman D, Schlumm D. Scripta Mater 2000;42(8):819–25.
[11] Collin M, Rowcliffe D. Acta Mater 2000;48(8):1655–65.
[12] Song F et al. Eur Phys Lett 2009;87(5):54001.
[13] Liu QN et al. Philos Mag 2010;90(13):1725–32.
[14] Liu QN et al. Chin Phys Lett 2010;27(8):088104.
[15] Han JC, Wang BL. Acta Mater 2011;59(4):1373–82.
[16] Bažant ZP, Ohtsubo H, Aoh K. Int J Fract 1979;15(5):443–56.
[17] Nemat-Nasser S. J Int Eng Sci 1978;16(4):277–85.
[18] Nemat-Nasser S et al. Int J Solids Struct 1978;14(6):409–30.
[19] Bahr HA, Fischer G, Weiss HJ. J Mater Sci 1986;21(8):2716–20.
[20] Bahr HA et al. Theor Appl Fract Mech 1987;8(1):33–9.
[21] Bahr HA et al. Theor Appl Fract Mech 1988;10(3):219–26.
[22] Jenkins DR. Phys Rev E 2005;71(5):056117.
[23] Bourdin B et al. J Elast 2008;91(1–3):5–148.
[24] Bourdin B. In: Combescure A, Belytschko T, de Borst R, editors. IUTAM symposium on discretization methods for evolving discontinuities. New York: Springer; 2007.
[25] Holman JP. Heat transfer. 9th ed. New York: McGraw-Hill; 2002.
[26] Zhang YL, Ma JP. Applicable ceramic material manual. Beijing: Chemical Industry Press; 2006 [in Chinese].
[27] Zhang QC. Mechanical properties of ceramics. Beijing: Science Press; 1987 [in Chinese].
[28] Fukuhara M, Yamauchi I. J Mater Sci 1993;28(17):4681–8.
[29] De Smet BJ, Bach PW. High temperature fracture toughness of alumina, ferrite and silicon carbide, ECN-C–92-083. Petten: ECN; 1992.
[30] Touloukian YS, Ho CY. Thermophysical properties of matter. Thermal conductivity of nonmetallic solids, vol. 2. New York: Plenum Press; 1972.
[31] Touloukian YS, Ho CY. Thermophysical properties of matter. Specific heat of nonmetallic solids, vol. 5. New York: Plenum Press; 1972.
[32] Jiang DL et al. China materials engineering canon. Beijing: Chemical Industry Press; 2006 [in Chinese].
[33] Singh JP, Tree Y, Hasselman DPH. J Mater Sci 1981;16(8):2109–18.
[34] Becher PF. J Am Ceram Soc 1981;64(1):C17–8.
[35] Kim Y, Lee WJ, Case ED. Mater Sci Eng A 1991;145(1):L7–L11.
[36] Lee WJ, Kim Y, Case ED. J Mater Sci 1993;28(8):2079–83.